

Perfluoro-Functionalized Conducting Polymers Enhance Electrocatalytic Oxygen Reduction

Tharwat Hassan Mansoure, Hailemichael Ayalew, Wei-Lun Kao, Jing-Jong Shyue, Shyh-Chyang Luo,* Yuan-Chung Cheng,* and Hsiao-hua Yu*

Cite This: *ACS Appl. Energy Mater.* 2020, 3, 1171–1180

Read Online

ACCESS |

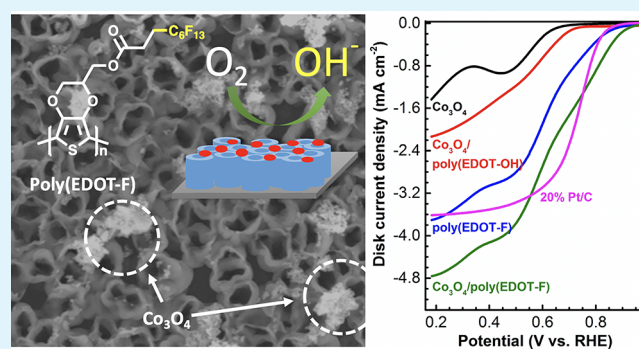
Metrics & More

Article Recommendations

Supporting Information

ABSTRACT: In this study, films of perfluoro-functionalized poly(3,4-ethylenedioxythiophene) [poly(EDOT-F)] were prepared directly through electropolymerization for use as catalysts for the oxygen reduction reaction (ORR), applying the rotating ring disk electrode technique. Poly(EDOT-F) operated catalytically through a two-electron and/or mixed pathway. Spinel Co_3O_4 nanospheres were introduced into poly(EDOT-F) to enhance its ORR performance and electron transfer number (n). Benefiting from its unique interconnected pore structure and its resemblance to the binder Nafion, poly(EDOT-F) could be used as a single replacement for both the binder and the carbon support required for the spinel Co_3O_4 nanospheres. The Co_3O_4 /poly(EDOT-F) composite, when used as an electrode, exhibited a limiting current density of $-4.761 \text{ mA cm}^{-2}$ at 0.18 V (vs RHE) (cf. 20% Pt/C: $-3.615 \text{ mA cm}^{-2}$), an onset potential of 0.99 V (cf. 20% Pt/C: 0.938 V), and a half-wave potential of 0.628 V (cf. 20% Pt/C: 0.727 V) in 0.1 M aqueous KOH. The electron transfer number of the Co_3O_4 /poly(EDOT-F) nanocomposite in the ORR was 3.84, suggesting a desirable four-electron pathway. This high electrocatalytic activity presumably resulted from the synergistic effect of the Co_3O_4 nanospheres and the poly(EDOT-F) polymer, which created many more active sites, enhanced the electron transfer kinetics, and eventually improved the ORR performance.

KEYWORDS: conducting polymer, perfluorocarbon, PEDOT, Co_3O_4 , oxygen reduction reaction



1. INTRODUCTION

Fossil fuels are of paramount importance to the global energy supply. Although relatively inexpensive, their combustion releases large quantities of CO_2 and other greenhouse gases into the atmosphere, arguably the main cause of climate change and global warming.^{1,2} Accordingly, there is enormous demand for clean and environmentally friendly alternatives to conventional fossil fuels, ideally renewable and functioning with lower CO_2 emissions. Among the most promising renewable energy technologies are fuel cells, which function with high energy densities, high efficiencies, and low CO_2 emissions. Fuel cells exploit the electrochemical oxidation of a fuel [e.g., H_2 on the anode, in the case of proton exchange membrane fuel cells (PEMFCs)] and reduction of an oxidant (e.g., O_2 on the cathode) to convert chemical energy into electrical energy (with water as the only emitted byproduct for PEMFCs).³ The sluggish nature of the reduction on the cathode in a PEMFC means, however, that the cathode requires a catalyst for the oxygen reduction reaction (ORR). Platinum dispersed on carbon (Pt/C) has, so far, been the most suitable catalyst for the ORR, exhibiting the highest electrocatalytic activity.^{4,5} Nevertheless, Pt/C catalysts have several drawbacks, including high cost, low tolerance to fuel/

methanol crossover, and low durability.⁶ To obviate these issues affecting the commercialization of PEMFCs, efforts are continuing to develop cost-effective, highly stable, and environmentally abundant nonplatinum and/or metal-free electrocatalysts for the ORR.^{7–10}

Several conducting polymers have been investigated as effective metal-free electrocatalysts for the ORR, including polypyrrole (PPy),^{11,12} polyaniline (PANI),^{13,14} and poly(3,4-ethylenedioxythiophene) (PEDOT).^{15,16} These polymers act not only as efficient ORR electrocatalysts but also as conductive supports (replacing the typically used carbon), as binders (replacing Nafion, the most commonly used material that accounts for almost 40% of the cost of the reaction cell), and as precursors for pyrolyzed M-Nx/C catalysts.^{11–25} PEDOT has received the most interest ever since Winther-Jensen observed its ability to catalyze the ORR.¹⁶ PEDOT is also used in many other electrochemical applications, including

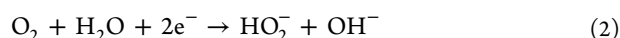
Received: November 14, 2019

Accepted: January 3, 2020

Published: January 3, 2020

sensors,²⁶ solar cells,²⁷ organic light-emitting diodes,²⁸ supercapacitors,²⁹ and Li-ion batteries^{30,31} because of its low cost, high electronic conductivity, good capacitive behavior, distinct redox properties, mechanical flexibility, and high chemical stability. In this regard, Winther-Jensen et al. revealed that vapor-phase-polymerized PEDOT on a porous GoreTex membrane exhibited high ORR performance, similar to that of Pt-catalyzed electrodes under parallel testing.¹⁶ In addition, Abdelhamid et al. found that the electropolymerized PEDOT, deposited from an ionic liquid (IL) in a sandwich configuration onto a flexible carbon cloth electrode, was active for the ORR over a wide pH range.²³ Moreover, introducing new functional groups to PEDOT enables tuning of its electrochemical properties.³² Nevertheless, the influence of such functional groups on the ORR performance has not been investigated previously. Consequently, in this study, two functionalized—hydroxyl and perfluoro—PEDOT derivatives were synthesized as new materials displaying excellent performance and tested for their use in the ORR. Their functionalization was performed through incorporation of the functional groups during the synthesis of their monomers.³³

The ORR proceeds generally through one of two pathways in alkaline media: (i) a four-electron pathway, in which each O₂ molecule is completely reduced to hydroxide (eq 1), or (ii) a two-electron pathway, in which each O₂ molecule is partially reduced to a hydrogen peroxide anion (HO₂⁻) (eq 2), which is then further reduced to hydroxide through another two-electron pathway (eq 3).^{15,34}



The electron transfer number (*n*) is a key parameter when assessing the ORR performance. A high value of *n* leads to the production of H₂O as the only byproduct (according to eq 1) without any H₂O₂, thereby protecting the PEMFC from deterioration. The literature suggests that the ORR at a PEDOT surface proceeds through the two overall pathways (i) and (ii), depending upon several factors, including the polymerization method (electro-, chemical-, or vapor-phase polymerization), morphology, synthesis solvent, and presence of metal oxides.^{15,18–20,23,35,36} For example, Abdelhamid et al. revealed that the ORR proceeds through the two-electron or mixed reduction pathway in an alkaline electrolyte at PEDOT [polymerized from the ionic liquid 1-butyl-1-methylpyrrolidinium bis(trifluoromethylsulfonyl)imide (C4mpyrTFSI)] in a sandwich configuration on flexible carbon cloth electrodes (*n* = 2.7).²³ Shi et al. reported that the ORR proceeds through the two-electron pathway at PEDOT:PSS (*n* = 2.0–2.2).³⁶ Moreover, Zhang et al. noted that the electron-transfer numbers for H₂SO₄-treated PEDOT:PSS/rGO composites were 3.3–3.8, significantly higher than those of PEDOT:PSS (2.0–2.2) and rGO (2.3–2.8) electrodes, the result of the increased conductivity of PEDOT and the further reduction of rGO by concentrated H₂SO₄.³⁶ Furthermore, Vigil et al. found that the incorporation of transition metal oxides (MnO_x, PdO_x) into PEDOT polymers increased the preference of the four-electron pathway, as well as the ORR performance, due to improved conductivity and electron transport.^{18–20}

The normal spinel tricobalt tetraoxide (Co₃O₄) nanostructure, with mixed oxidation states of Co²⁺ (3d⁷) occupying

tetrahedral sites and Co³⁺ (3d⁶) occupying octahedral sites, is one of the most promising alternatives to platinum and rare metal oxides (e.g., RuO₂, IrO₂) for use as a catalyst for the ORR due to its low cost, excellent catalytic properties, earth-abundance, and high corrosion stability.^{7–9} Nanostructured Co₃O₄ has been applied in many fields, including lithium-ion batteries, electrochemical capacitors, electrochromic devices, gas sensors, and catalysts.^{37–45} In addition, Co₃O₄ nanostructures of various morphologies, including nanospheres,⁴⁶ nanocubes,^{47,48} nanoparticles,^{45,49} nanoflakes,⁴² nanowires,^{39,50} nanorods,^{51,52} and nanosheets,⁵³ have been examined for the ORR. Typically, these nanostructures have been deposited on the working electrodes using conventional methods (drop-casting) that require ancillary materials (binders), thereby decreasing the electrocatalytic activity of the nanostructured Co₃O₄ toward the ORR.^{50,53,54} Moreover, the electrocatalytic performance of the nanostructured Co₃O₄ is affected by its poor electric conductivity, which may, however, be improved through support on a conducting material.^{49,46} Therefore, combining Co₃O₄ nanospheres with PEDOT-based polymers might be an effective strategy for merging all of these attractive features and fulfilling the requirements for high-performance nanocomposite electrode materials for the ORR: a greatly increased number of surface active sites, strong synergetic coupling, and enhanced electron transfer.

In this study, pure PEDOT and two functionalized PEDOTs—namely hydroxymethyl and perfluoro-functionalized PEDOTs [poly(EDOT-OH) and poly(EDOT-F), respectively; Figure 1]—were prepared as nanostructured

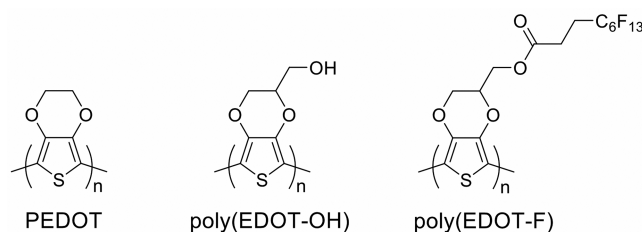


Figure 1. Molecular structures and abbreviated names of the (functionalized) PEDOTs used in this study.

materials through facile syntheses involving electropolymerization onto glassy carbon from CH₂Cl₂ solutions containing tetrabutylammonium hexafluorophosphate (Bu₄NPF₆) as a supporting electrolyte at an anodic potential. These functional groups provided not only different chemical structures but also different surface properties: the hydroxymethyl groups provided a hydrophilic surface, and the perfluorocarbon groups provided a superhydrophobic surface. To the best of our knowledge, functionalized nanostructured PEDOT polymers have not been investigated previously as cathode catalysts for the electrocatalytic ORR. Therefore, the influence of these functional groups on the ORR performance was examined. Each of these polymers functioned catalytically through a two-electron and/or mixed pathway. Subsequent blending of the nanostructured Co₃O₄ with the pure and functionalized PEDOT-based conducting polymers greatly promoted the preference for the four-electron mechanism, the result of improvements in the electrochemical surface area and the electron transport. Indeed, the Co₃O₄/poly(EDOT-F) nanocomposite exhibited a four-electron pathway with a value of *n* of 3.84.

2. RESULTS AND DISCUSSION

2.1. Characterization of Catalysts. Field emission scanning electron microscopy (FE-SEM) images were recorded to examine the morphologies of the polymers. Figure 2 presents SEM images of the electropolymerized PEDOT,

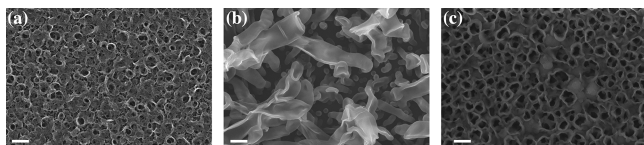


Figure 2. FE-SEM images of electropolymerized (a) PEDOT, (b) poly(EDOT-OH), and (c) poly(EDOT-F) on glassy carbon substrates. Scale bar: 1 μm .

poly(EDOT-OH), and poly(EDOT-F) nanostructures on glassy carbon substrates. The morphologies were, in general, tubular and/or interconnected pores, with the degrees of ordering and density depending on the functional group attached to the monomer. PEDOT formed an interconnected pore structure having a small pore length with some of its pores blocked (Figure 2a); poly(EDOT-OH) formed randomly distributed nanotubes with lower degrees of ordering and density (Figure 2b), and poly(EDOT-F) formed uniform interconnected pore structures with well-ordered longer pore length, very thin walls, and higher density (Figure 2c). To explore how the functional groups affected the shapes and lengths of these structures, the electropolymerization current–time ($I-t$) curves of PEDOT, poly(EDOT-OH), and poly(EDOT-F) obtained under a constant applied voltage of +1.4 V (vs Ag/Ag⁺) at 25 °C were recorded (Figure S1). The electropolymerization currents decreased in the order poly(EDOT-OH) > PEDOT > poly(EDOT-F) (Figure S1). For PEDOT, the electropolymerization current initially decreased slightly upon increasing the time due to the limited supply of monomers through diffusion, indicative of fast polymerization. Interconnected pores formed in this case as a result of the rapid rate of polymerization and the insufficient monomer supply.⁵⁵ Thereafter, the electropolymerization current increased slightly, suggesting a sufficient supply of diffusing monomers; that is, at this point, the monomers in the bulk solution had sufficient time to diffuse into and block some pores.⁵⁵ Functionalization of EDOT with a hydroxymethyl group gave the monomer EDOT-OH, for which the electropolymerization rate increased and the polymerization time decreased (Figure S1). Therefore, the hydroxyl functional groups of the EDOT-OH monomer facilitated its electropolymerization to poly(EDOT-OH) while also affecting the polymer growth and morphology. Accordingly, we observed randomly distributed, less-dense, and less-ordered nanotubes, presumably the result of much higher rates of electropolymerization and sufficient supplies of monomers—that is, there was not enough time for the growth and formation of uniform, well-ordered nanotubes. Further functionalization of EDOT-OH with a perfluoro unit gave the monomer EDOT-F; the presence of its bulky side chain decreased the polymerization rate and increased the polymerization time (Figure S1). Therefore, the EDOT-F monomers had sufficient time to diffuse from the bulk solution. Accordingly, poly(EDOT-F) formed uniform interconnected pore structures with well-ordered longer pore length, very thin walls, and high

density. The shapes and lengths of these structures were all dependent on the functional groups present in the monomers.

Figure 3 presents SEM images of the Co₃O₄/PEDOT, Co₃O₄/poly(EDOT-OH), and Co₃O₄/poly(EDOT-F) nano-

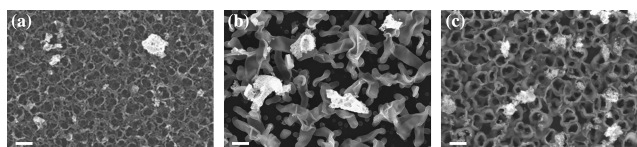


Figure 3. FE-SEM images of (a) Co₃O₄/PEDOT, (b) Co₃O₄/poly(EDOT-OH), and (c) Co₃O₄/poly(EDOT-F) on glassy carbon substrates. Scale bar: 1 μm .

composites on glassy carbon substrates; Figure S2 displays X-ray diffraction (XRD) patterns of the Co₃O₄ nanoparticles, while Figure S3 presents high-magnification SEM and transmission electron microscopy (TEM) images of the pure Co₃O₄ nanoparticles and Co₃O₄/poly(EDOT-F) nanocomposite. The formation of the Co₃O₄ nanoparticles was confirmed from the XRD data.^{46,52} The diffraction peaks of the Co₃O₄ nanoparticles were in good agreement with those of the standard Co₃O₄ (JCPDS card: 42-1467). The Co₃O₄ nanoparticles appear to be homogeneously distributed on the polymers in Figures 3a–c due to the homogeneous distribution of the functional groups on the polymers' surfaces acting as anchoring sites for the Co₃O₄ nanoparticles. High-magnification SEM images (Figure S3a and S3b) revealed spherical structures for the pure and supported Co₃O₄ nanoparticles with diameters of 15–36 nm. Moreover, Figure 3c reveals that the Co₃O₄ nanoparticles filled the pores of poly(EDOT-F) polymer. We estimated the pore diameters of poly(EDOT-F) to be within the range 300–600 nm. The TEM image revealed a spherical morphology for the pure crystalline spinel Co₃O₄ nanocrystals with an approximate diameter of 15–36 nm (Figure S3c).

X-ray photoelectron spectroscopy (XPS) was used to characterize the chemical structure of the Co₃O₄/poly(EDOT-F) nanocomposite. Figure 4a presents the XPS survey spectrum of the Co₃O₄/poly(EDOT-F) nanocomposite catalyst. The XPS full spectrum featured signals for the elements Co, F, S, O, and C along with Co, O, and F Auger peaks, confirming the existence of both Co₃O₄ and poly(EDOT-F) in the catalyst sample.^{7,30,56–62} An XPS depth-profile revealed the variations in the atomic concentrations of the elements Co, F, S, and O in the Co₃O₄/poly(EDOT-F) catalyst layers. To obtain the depth profile, XPS spectra were recorded after subjecting the Co₃O₄/poly(EDOT-F) layers to a series of Ar⁺ ion beam etchings. Figure 4b reveals that the atomic concentrations of Co 2p, F 1s, S 2p, and O 1s all decreased continuously upon increasing the sputter time [0–205 min; the latter resulting in the removal of ca. 93% of the Co₃O₄/poly(EDOT-F)] as the XPS measurement point approached the glassy carbon substrate. This behavior suggests that the Co₃O₄ nanoparticles were uniformly and homogeneously distributed within the pores of the polymer; therefore, the Co₃O₄/poly(EDOT-F) nanocomposite catalyst could be considered as featuring just one layer, rather than two.

Figures 4c and 4d and Figures S4a and S4b provide characteristic high-resolution Co 2p, F 1s, S 2p, and O 1s XPS spectra, respectively, recorded from the Co₃O₄/poly(EDOT-F) catalyst surface before and after sputtering with an Ar⁺ ion

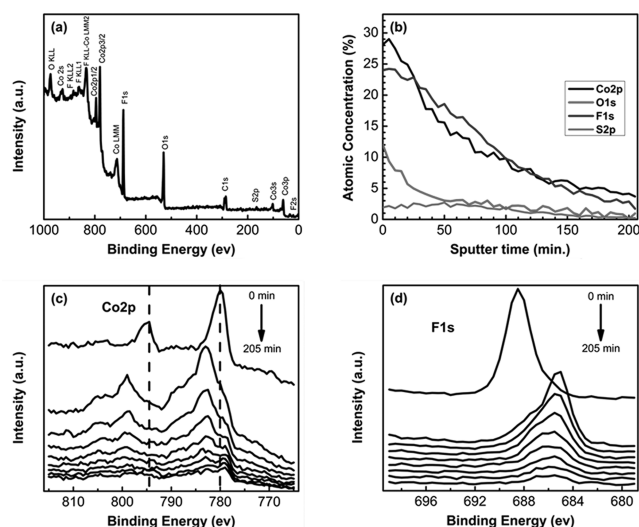


Figure 4. (a) XPS survey spectrum of the $\text{Co}_3\text{O}_4/\text{poly}(\text{EDOT-F})$ nanocomposite catalyst. (b–d) Depth profiles of the $\text{Co}_3\text{O}_4/\text{poly}(\text{EDOT-F})$ nanocomposite catalyst after Ar^+ ion beam etching: (b) atomic ratio profile of each element in each layer after exposure for various etching times; (c) Co 2p and (d) F 1s regions.

gun for various times. Apparent differences appeared in the spectra for these characteristic signals. Prior to etching, the XPS spectrum for Co 2p (Figure 4c) featured two major peaks with binding energies centered at 780 and 794.5 eV, corresponding to Co 2p_{3/2} and Co 2p_{1/2}, respectively, with a spin-energy separation of 14.5 eV, which is characteristic of a spinel Co_3O_4 phase, in good accordance with the XRD data (Figure S2).^{7,9,46,52} In addition, weak 2p satellite features for the Co_3O_4 spinel appeared near 789 and 805 eV, characteristic of a spinel structure in which Co^{3+} cations occupy octahedral lattice sites and Co^{2+} cations occupy tetrahedral sites.^{39,50} After etching with Ar^+ ions, the positions of the Co 2p peaks shifted to slightly higher binding energies (centered at 783 and 799 eV, with a spin-energy separation of 16 eV); in addition, the peak heights decreased continuously upon increasing the sputter time. Moreover, the Co 2p peaks exhibited two intense satellite peaks at lower binding energies of 788.5 and 803.5 eV, attributable to the Co^{2+} oxidation state, suggesting that a portion of the Co^{3+} ions had been reduced to Co^{2+} and formed new oxygen vacancies, consistent with previous reports of the conversion of Co_3O_4 to CoO upon Ar^+ ion sputtering.^{39,56,57} Co atoms were, however, detected, even near the substrate, suggesting that Co_3O_4 diffused into the pores of the poly(EDOT-F) polymer.

Figure 4d presents the F 1s XPS spectra of the $\text{Co}_3\text{O}_4/\text{poly}(\text{EDOT-F})$ nanocomposite catalyst. Although fluorine has different binding energies in different polymers, F 1s is very symmetrical and always fittable by a single component. Prior to etching, the spectrum exhibited one major peak having a binding energy centered at 688.5 eV, corresponding to the fluorine atoms of poly(EDOT-F), presumably C–F semi-ionic-bonded fluorine atoms.^{58,59} Figure 4d reveals that the fluorine signal from poly(EDOT-F) appeared at the surface of the $\text{Co}_3\text{O}_4/\text{poly}(\text{EDOT-F})$ nanocomposite catalyst, indicating that the Co_3O_4 nanoparticles did not block the polymer layer but had instead entered the pores of the polymer. After etching with Ar^+ ions, the F 1s peak shifted to a lower binding energy centered at 685 eV, corresponding to C–F ionic-bonded fluorine atoms;⁶³ thus, etching with Ar^+ ions converted the C–

F semi-ionic bonding into ionic bonding. In addition, the peak heights decreased continuously upon etching, consistent with the removal of some polymer layers. In this regard, Lee et al. demonstrated that the fluorine atoms induce the carbon atoms to possess a positive charge and improve the activity of the π -electrons of the carbon atoms, resulting in improved adsorption of oxygen and enhanced ORR activity.⁶⁴ In addition, Panomsuwan et al. concluded that fluorine atoms bonded to carbon atoms of ionic and semi-ionic types play the role of electron acceptors, thereby facilitating charge transfer between the fluorine and carbon atoms and enhancing the conductivity and modifying the electronic properties of the pristine carbon atoms.⁶⁵ Therefore, the tubular morphology and the active semi-ionic C–F bonds would be expected to enhance the ORR performance of both the poly(EDOT-F) polymer and $\text{Co}_3\text{O}_4/\text{poly}(\text{EDOT-F})$ nanocomposites.

Figure S4a provides the S 2p XPS spectra of the $\text{Co}_3\text{O}_4/\text{poly}(\text{EDOT-F})$ nanocomposite catalyst. Prior to etching, the spectrum featured two major peaks with binding energies centered at 163.5 and 165 eV, corresponding to the sulfur atoms of poly(EDOT-F).^{10,23,30} After etching with Ar^+ ions, the S 2p peak centered at 165 eV shifted to slightly lower binding energy centered at 164 eV. In addition, the peak heights decreased continuously upon etching, suggesting the removal of sulfur-containing functional groups. Figure S4b displays the O 1s XPS spectra of the $\text{Co}_3\text{O}_4/\text{poly}(\text{EDOT-F})$ nanocomposite catalyst. Prior to etching, the spectrum exhibited two peaks with binding energies centered at 530 and 533 eV, corresponding to the oxygen atoms of the $\text{Co}_3\text{O}_4/\text{poly}(\text{EDOT-F})$ nanocomposite catalyst. The signal at 530 eV originated from the Co–O bonds of the spinel Co_3O_4 oxide,^{8,53,56,57} while the signal centered at 533 eV reflected the *O=C-O , O=C-O* , and C–O bonds of poly(EDOT-F).³⁰ After etching with Ar^+ ions, the peak heights decreased, indicative of the removal of oxygen-containing functional groups.

2.2. Electrocatalytic ORR Performance. Cyclic voltammetry (CV) and linear sweep voltammetry (LSV) were used to evaluate the ORR electrocatalytic performances of the PEDOT, poly(EDOT–OH), and poly(EDOT-F) polymer samples. Stable CV curves were recorded in the potential range from 0.1 to 1.1 V (vs RHE) at 100 mV s^{-1} in 0.1 M KOH saturated with either N_2 or O_2 . Figure 5 presents the CV curves

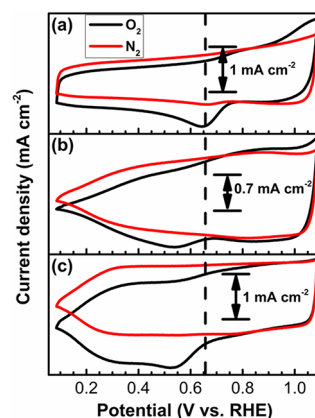


Figure 5. CV curves of the (a) PEDOT, (b) poly(EDOT–OH), and poly(EDOT-F) polymer catalysts on a glassy carbon RRDE in N_2 (red line)- and O_2 (black line)-saturated 0.1 M KOH (scan rate: 100 mV s^{-1}).

of the electropolymerized PEDOT, poly(EDOT–OH), and poly(EDOT–F) nanostructures on the glassy carbon rotating ring disk electrode (RRDE). The ORR peak potentials and water contact angles of the tested polymers are listed in Table 1. Featureless voltammetric currents were observed for the

Table 1. ORR Peak Potentials Obtained from CV Curves (Figure 5); Limiting Current Densities (I_L), Half-Wave Potentials ($E_{1/2}$), and Onset Potentials Obtained from LSV Curves (Figure 6a); and Contact Angles of Water Droplets on PEDOT and Functionalized PEDOTs Prepared through Electropolymerization on Glassy Carbon Substrates

polymer	peak potential (V)	I_L (mA cm^{-2})	$E_{1/2}$ (V)	onset potential (V)	CA_{water} ($^\circ$)
PEDOT	0.641	−2.329	0.625	0.810	55.6
poly(EDOT–OH)	0.536	−1.996	0.525	0.750	23.5
poly(EDOT–F)	0.524	−3.707	0.603	0.982	154
Co_3O_4		−1.434	0.522	0.720	
$\text{Co}_3\text{O}_4/\text{PEDOT}$		−2.592	0.664	0.830	
$\text{Co}_3\text{O}_4/\text{poly(EDOT–OH)}$		−2.135	0.525	0.770	
$\text{Co}_3\text{O}_4/\text{poly(EDOT–F)}$		−4.761	0.628	0.990	
20% Pt/C		−3.615	0.727	0.938	

tested polymer samples in the N_2 -saturated solutions (Figure 5). In contrast, single broad cathodic peaks corresponding to the ORR appeared for all of the polymer samples in the O_2 -saturated solutions (Figure 5). PEDOT displayed the most positive ORR peak potential of 0.641 V (vs RHE) (Table 1). After functionalization of PEDOT, the ORR peak shifted to a slightly more negative potential, decreasing in the order PEDOT > poly(EDOT–OH) > poly(EDOT–F) (Table 1).

To gain further insight into the electrocatalytic activity for the ORR, LSV measurements on an RRDE were performed in O_2 -saturated 0.1 M KOH at a scan rate of 10 mV s^{-1} at a rotation rate of 1600 rpm (Figure 6a). The characteristic parameters for the ORR performance—the limiting current density (I_L), half-wave potential ($E_{1/2}$), and the onset potential—obtained from the LSV curves at 1600 rpm are listed in Table 1. The ORR activity increased in the order poly(EDOT–OH) < PEDOT < poly(EDOT–F), as evidenced from the limiting current densities for the ORRs of these polymers (Figure 6a). Functionalization of EDOT with a hydroxymethyl group shifted the half-wave potential to more negative value and decreased the limiting current density ($E_{1/2}$: 0.525 V vs RHE; I_L : $-1.996 \text{ mA cm}^{-2}$) relative to those of PEDOT (0.625 V and $-2.329 \text{ mA cm}^{-2}$, respectively). Further functionalization of hydroxymethyl-EDOT with long-chain perfluoro units shifted the half-wave potential to a more positive value and increased the limiting current density ($E_{1/2}$: 0.603 V vs RHE; I_L : $-3.707 \text{ mA cm}^{-2}$) when compared with those of poly(EDOT–OH). In addition, the onset potential (E_{onset} : 0.982 V vs RHE) of poly(EDOT–F) was much more positive than those of PEDOT (0.810 V) and poly(EDOT–OH) (0.750 V), reflecting the improved ORR performance for poly(EDOT–F) with respect to the other tested polymers. We attribute the slight decrease in ORR performance after hydroxymethyl functionalization to (i) the shifting of the

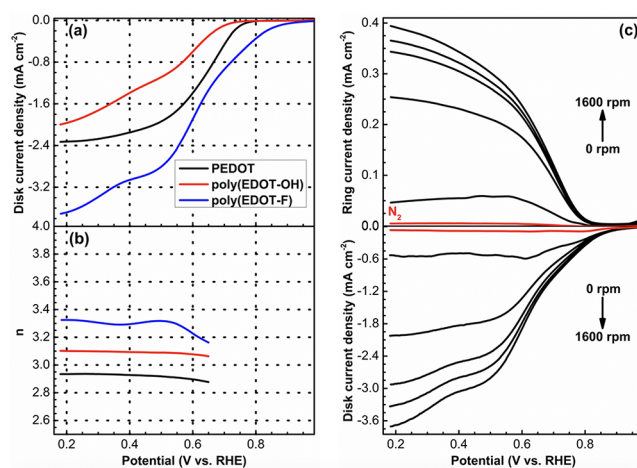


Figure 6. (a) LSV curves of nonfunctionalized and functionalized PEDOT polymer catalysts on a glassy carbon RRDE in O_2 -saturated 0.1 M KOH (scan rate: 10 mV s^{-1} ; rotation rate: 1600 rpm). (b) Electron transfer numbers (n) calculated at various potentials based on corresponding RRDE data. (c) LSV curves of poly(EDOT–F) recorded at various rotation rates (0, 400, 900, 1200, 1600) in O_2 - and N_2 -saturated 0.1 M KOH (scan rate: 10 mV s^{-1}).

ORR peak potential to a more negative value, relative to that for PEDOT (Table 1), and (ii) poly(EDOT–OH) comprising randomly distributed, less-dense, and less-ordered nanotubes, accompanied by losses in porosity and a decrease in the number of active sites (as revealed through SEM imaging). Moreover, the observed ORR behavior over poly(EDOT–F) could be imputed by the following factors. First, as SEM revealed, poly(EDOT–F) possessed a uniform interconnected pore structure with well-ordered longer pore length, which would promote O_2 diffusion, facilitate electron transport, and suppress Ostwald ripening, eventually enhancing the ORR performance.⁶⁶ Second, as confirmed through XPS analysis, the fluorine atoms induced C–F semi-ionic active units. Previous reports have stated that semi-ionic C–F bonds are more active toward the ORR than are covalent C–F bonds^{58,64,65} in terms of (i) highly increased adsorption of oxygen and (ii) activation of O–O bond cleavage.^{64,65} Thus, the presence of fluorine atoms in poly(EDOT–F), in the form of active C–F semi-ionic bonds, affected the polymer's electronic structure and created new active sites for the ORR on the catalyst.

The quantification of the ring and disk currents induced by the RRDE allowed accurate calculations of the values of n and the intermediate peroxide percentages ($\%\text{HO}_2^-$) based on the collection efficiency of the instrument. The number of electrons transferred (n) for the ORR at 1600 rpm (Figure 6b) and the corresponding values of $\%\text{HO}_2^-$ produced at the disk electrode (Figure S5) were calculated using eqs 6 and 7, respectively. The calculated value of n during the ORR decreased in the order poly(EDOT–F) > poly(EDOT–OH) > PEDOT (Figure 6b); the corresponding values of $\%\text{HO}_2^-$ produced at the disk electrode increased in the same order (Figure S5). These results imply that the ORR processes occurring at the investigated polymer electrodes proceeded through two-electron and/or mixed pathways. Accordingly, spinel Co_3O_4 nanospheres were introduced into these polymers to enhance their ORR performance and their preference for the four-electron pathway. Figure 6c presents the ring (j_R) and disk (j_D) current densities obtained from the LSV curves of poly(EDOT–F) measured at rotation speeds of

0, 400, 900, 1200, and 1600 rpm in O₂- and N₂-saturated 0.1 M KOH. The LSV curves of PEDOT and poly(EDOT-OH) electrodes in O₂-saturated 0.1 M KOH, measured at a scan rate of 10 mV s⁻¹ and various electrode rotating speeds, are provided in the Supporting Information (Figures S6 and S7, respectively).

Figure 7a presents the LSV curves of pure and supported Co₃O₄-functionalized PEDOT catalysts on a glassy carbon

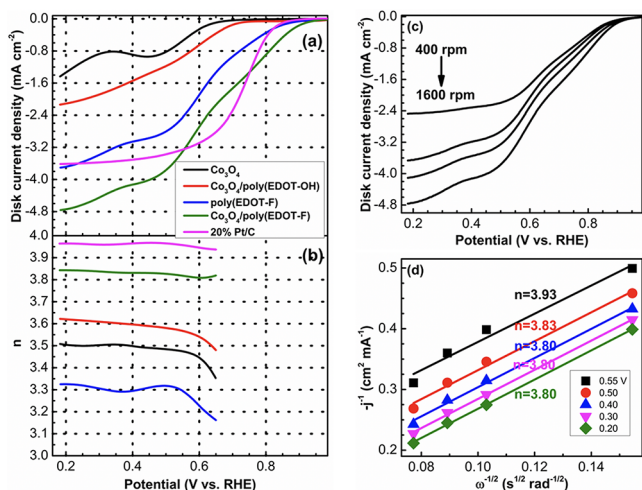


Figure 7. (a) LSV curves of pure poly(EDOT-F), Co₃O₄, 20% Pt/C, and Co₃O₄-supported functionalized PEDOT catalysts on a glassy carbon RRDE in O₂-saturated 0.1 M KOH (scan rate: 10 mV s⁻¹; rotation rate: 1600 rpm). (b) Electron transfer numbers (n) calculated at various potentials. (c) LSV curves of Co₃O₄/poly(EDOT-F) nanocomposite catalyst measured at various electrode rotating rates in O₂-saturated 0.1 M KOH (scan rate: 10 mV s⁻¹). (d) Koutecky–Levich plots for the Co₃O₄/poly(EDOT-F) nanocomposite catalyst measured at various electrode potentials.

RRDE in O₂-saturated 0.1 M KOH. Table 1 lists the half-wave potentials ($E_{1/2}$), onset potentials, and limiting current densities (I_L) obtained from the LSV curves at 1600 rpm. Figure S8 presents the LSV curves of Co₃O₄/PEDOT measured at various rotation rates in O₂- and N₂-saturated 0.1 M KOH. The ORR performance improved after the addition of the Co₃O₄ nanostructures to the pure and functionalized PEDOT polymers in terms of increasing the limiting current density and shifting the onset and half-wave potentials to more positive values (Table 1). In addition, the ORR activity increased in the order Co₃O₄ < Co₃O₄/poly(EDOT-OH) < Co₃O₄/PEDOT < poly(EDOT-F) \approx 20% Pt/C < Co₃O₄/poly(EDOT-F), as evidenced by the limiting current densities for the ORRs of these samples (Figures 7a and S8). The improvement in the ORR performance of the Co₃O₄/poly(EDOT-F) nanocomposite is evidenced by the improvements in the limiting current density (Co₃O₄: -1.434 mA cm⁻²; poly(EDOT-F): -3.707 mA cm⁻²; Co₃O₄/poly(EDOT-F): -4.761 mA cm⁻²), the half-wave potential (Co₃O₄: 0.522 V vs RHE; poly(EDOT-F): 0.603 V; Co₃O₄/poly(EDOT-F): 0.628 V), and the onset potential (Co₃O₄: 0.720 V; poly(EDOT-F): 0.982 V; Co₃O₄/poly(EDOT-F): 0.990 V). In addition, the performance of Co₃O₄/poly(EDOT-F) was better than that of the commercial benchmark catalyst 20% Pt/C, which exhibited an onset potential of 0.938 V vs RHE and a limiting current density of -3.615 mA cm⁻². The addition of Co₃O₄ created new active

sites for the ORR process on the catalysts. Here, the polymer poly(EDOT-F) acted not only as a conducting matrix but also as a binder for the nanostructured Co₃O₄. The electrochemical active surface areas (ECSAs) for poly(EDOT-F) and Co₃O₄/poly(EDOT-F) were estimated by determining the double-layer capacitance (C_{DL}) from the CV traces using the equation

$$ECSA = C_{DL}/C_S \quad (4)$$

where C_S is the specific capacitance.⁶⁷ Because the specific capacitance is not known for the Co₃O₄/poly(EDOT-F) nanocomposite, we chose to report the double-layer capacitance (C_{DL}) as an approximation of the surface area accessible to the electrolyte and, thus, available for catalysis. Figure S9 presents the results of repeated CV scans in a 0.1-V non-Faradaic potential window, from 0.957 to 0.857 V vs RHE, at increasing scan rates. The values of C_{DL} , calculated from the slopes of the correlations between the current near the switching potential (0.9 V vs RHE) and the scan rate (Figure S9), were 8.74 mA cm⁻² for Co₃O₄/poly(EDOT-F) and 8.10 mA cm⁻² for poly(EDOT-F). Table S1 provides a comparison of the ORR performances with those of all of the other studied PEDOT and PEDOT composite catalysts. These data reveal the superior performance of the Co₃O₄/poly(EDOT-F) electrocatalyst when compared with other PEDOT-based ORR electrocatalysts.

Figure 7b displays the calculated electron-transfer numbers (n) for the ORRs at the pure and supported Co₃O₄-functionalized PEDOT polymer catalysts at 1600 rpm; Figure S10 provides the corresponding peroxide percentages (% HO₂⁻). The electron-transfer numbers (n) for the ORR at the pure nanostructured Co₃O₄ (ca. 3.35–3.50) were higher than those at the functionalized PEDOT polymers (Figure 6b). Moreover, the values of n for the ORR at the Co₃O₄/poly(EDOT-F) nanocomposite catalyst (3.80–3.84) were higher than those at the pure poly(EDOT-F) (3.20–3.33) and Co₃O₄ (3.35–3.5) as well as those at the Co₃O₄/PEDOT (3.37–3.41) and Co₃O₄/poly(EDOT-OH) (3.48–3.62) nanocomposites. Thus, the ORR process at the Co₃O₄/poly(EDOT-F) nanocomposite electrode followed a four-electron pathway, whereas mixed pathways dominated the ORR reactions at the Co₃O₄, poly(EDOT-F), Co₃O₄/PEDOT, and Co₃O₄/poly(EDOT-OH) electrodes.

Figure 7c presents the disk current densities (j_D) obtained from the LSV curves of Co₃O₄/poly(EDOT-F) measured at rotation rates of 400, 900, 1200, and 1600 rpm in O₂-saturated 0.1 M KOH. Figure 7d displays corresponding Koutecky–Levich plots obtained from the inverse current density (j^{-1}) with respect to the inverse of the square root of the rotation rate ($\omega^{-1/2}$) for Co₃O₄/poly(EDOT-F) at 0.55, 0.50, 0.40, 0.30, and 0.20 V vs RHE. These plots are linear and parallel, indicating the first-order dependence of the kinetics of the ORR on the Co₃O₄/poly(EDOT-F) surface.^{50,52} Each straight line intercept corresponds to the kinetic current density (j_k). The “B-factor” for Co₃O₄/poly(EDOT-F) was 0.420 mA cm⁻² s^{1/2} rad^{-1/2}, determined from the slopes of the Koutecky–Levich plots. The electron-transfer numbers n calculated from the B-factor were in the range 3.8–3.93. This range is consistent with that (ca. 3.8–3.84) obtained from the RRDE measurements, suggesting that Co₃O₄/poly(EDOT-F) favored a four-electron reduction reaction process.

The stability of a catalyst is an important parameter affecting its practical application in fuel cells. Figures 8 and S12 present the stabilities of the 20% Pt/C, Co₃O₄/poly(EDOT-F), and

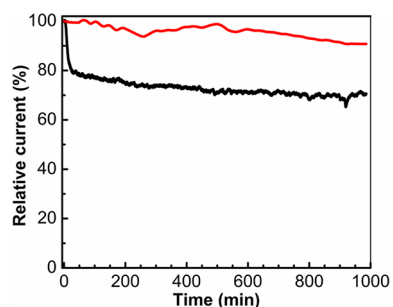


Figure 8. Current–time (I – t) chronoamperometric responses for ORRs on 20% Pt/C (black line) and Co_3O_4 /poly(EDOT-F) (red line) in O_2 -saturated 0.1 M KOH at +0.4 V (vs RHE); rotating rate: 1600 rpm.

poly(EDOT-F) catalysts for the ORR, assessed through chronoamperometric tests performed at 0.4 V (vs RHE) in O_2 -saturated 0.1 M KOH at a rotation rate of 1600 rpm. The Co_3O_4 /poly(EDOT-F) nanocomposite exhibited a very slight decrease in current after 16 h with a high current retention of 90.8%. In contrast, 20% Pt/C exhibited a much more rapid decrease in current, with only 70% retention. Thus, the Co_3O_4 /poly(EDOT-F) electrocatalyst was much more stable than the 20% Pt/C catalyst. Therefore, the observed improvement in ORR performance at the Co_3O_4 /poly(EDOT-F) electrode, with the preference for a four-electron pathway and excellent durability, was presumably due to the existence of many more active sites after the addition of Co_3O_4 because the ECSA had increased and because the unique tubular structure of the polymer poly(EDOT-F) provided higher conductivity (thereby improving the electron transfer kinetics), synergistically enhancing the electrocatalytic activity.

3. CONCLUSIONS

Parent and two functionalized PEDOT derivatives, hydroxymethyl and perfluoro, were prepared directly through simple and facile electropolymerization from corresponding monomers, providing new materials displaying excellent performance, and tested in ORRs. Each of these polymers functioned catalytically through a two-electron and/or mixed pathway. To enhance the number of electrons transferred (n), Co_3O_4 /polymer composites were prepared and tested for their ORR performance. SEM and XPS analyses revealed that the Co_3O_4 nanospheres filled the pores of the tubular structure of the polymer poly(EDOT-F). The ORR performance and durability of the Co_3O_4 /poly(EDOT-F) nanocomposite catalyst were significantly greater than those of the individual Co_3O_4 and poly(EDOT-F). Notably, the ORR performance at the Co_3O_4 /poly(EDOT-F) nanocomposite electrode was almost the result of a four-electron pathway, whereas mixed pathways dominated the ORR reactions on the individual Co_3O_4 and poly(EDOT-F). This behavior was due mainly to the synergistic effect of Co_3O_4 and poly(EDOT-F), creating many more active sites, enhancing the electron transfer kinetics, and eventually improving the ORR performance.

4. EXPERIMENTAL SECTION

4.1. Materials. Cobalt nitrate hexahydrate $\text{Co}(\text{NO}_3)_2 \cdot 6\text{H}_2\text{O}$ (Alfa Aesar), commercial benchmark electrocatalyst powder 20% Pt/C (Aldrich), glycine (J. T. Baker), 3,4-ethylenedioxythiophene (EDOT; Aldrich), and hydroxymethyl-EDOT (EDOT-OH; Aldrich) were used as received unless otherwise noted.

4.2. Synthetic Procedures. Co_3O_4 Nanoparticles. Co_3O_4 nanospheres were prepared through a facile combustion method, as described previously.⁶⁸ In a typical synthesis, $\text{Co}(\text{NO}_3)_2 \cdot 6\text{H}_2\text{O}$ (12.5 mmol) and glycine (6.25 mmol) were dissolved in distilled water (100 mL) to form a pink homogeneous solution, which was then heated on a hot plate (ca. 100 °C) to evaporate the excess water. The resulting viscous gel was calcined in a muffle furnace (400 °C, 3 h) under a static air atmosphere.

EDOT-F Monomer. The synthesis of the EDOT-F monomer, following a previously published synthetic procedure,⁶⁹ is provided in the Supporting Information.

4.3. Electropolymerization. The electropolymerization was implemented using a potentiostat (PGSTAT204, Autolab) with a glassy carbon electrode (GCE) as a working electrode, a Ag/Ag^+ electrode (RE-7, BAS) as the reference electrode, and a Pt wire as the counter electrode. Prior to use, the GCE was polished several times with 0.05- μm alumina powder, washed with EtOH after each polishing step, cleaned through sonication (5 min) in a water bath, washed with EtOH, and then dried in air. The ORR catalytic activity was first measured over the pure polymers (without Co_3O_4) and then over the Co_3O_4 /polymer nanocomposite catalysts. For the pure polymers, the working electrodes were prepared as follows: nanostructured EDOTs and their functionalized monomers were polymerized potentiostatically on the disk electrode of a RRDE from a 10 mM solution of the particular monomer in CH_2Cl_2 in the presence of 100 mM Bu_4NPF_6 as a supporting electrolyte. Chronoamperometric methods were used for electropolymerization of the EDOTs and their functionalized monomers by applying a constant voltage (+1.40 V vs Ag/Ag^+) and constant polymerization charge ($Q = 0.121 \text{ C cm}^{-2}$). The number of moles of the polymer film was controlled by fixing the total charge passed during the electropolymerization process. After polymerization, the obtained polymer electrodes were washed repeatedly with monomer-free MeCN to remove residual monomer and electrolyte from the electrode surface.

For the Co_3O_4 /polymer nanocomposite catalysts, the Co_3O_4 catalyst ink was prepared as follows: Co_3O_4 (8 mg) was dispersed in EtOH [(7.920 mL of EtOH + 0.080 mL of Nafion) for PEDOT and poly(EDOT-OH); (8 mL of EtOH) for poly(EDOT-F)] until a homogeneous mixture formed. After sonication (30 min), a portion (10 μL) of the suspension was pipetted out and drop-cast onto the polymer-coated glassy carbon surface and dried in air at room temperature for 1 h. The catalyst loading was calculated to be 40.4 $\mu\text{g cm}^{-2}$ for each of the tests.

Twenty percent Pt/C catalyst ink was prepared as follows: 20% Pt/C powder (2 mg) was dispersed in EtOH (1.980 mL) and Nafion solution (0.020 mL). After sonication (30 min), a portion (10 μL) of the suspension was pipetted out and drop-cast onto the glassy carbon surface and dried in air at room temperature for 1 h.

4.4. Materials Characterization. The morphologies of the polymers and Co_3O_4 -supported polymer nanocomposites were observed through FE-SEM (ZEISS ULTRA PLUS) at an accelerating voltage of 10 kV. TEM images were recorded using a JEOL JEM-1400 microscope operated at 120 kV. Crystal structures were determined through XRD using a Bruker D8 Advance instrument and $\text{Cu K}\alpha$ radiation ($\lambda = 1.5418 \text{ \AA}$) at 40 kV and 40 mA with a scanning rate (in 2θ) of 0.02 min^{-1} ; the XRD data are presented in the Supporting Information (Figure S1). XPS was performed using a PHI 5000 VersaProbe III spectrometer and a monochromatic Al $\text{K}\alpha$ source (1486.6 eV) operated at 50 W under a vacuum of 10^{-8} Pa in the analyzer chamber. High-resolution spectra of powdered samples were recorded at a takeoff angle of 45° with a constant pass energy of 93.9 eV using a 100- μm -diameter analysis area; a pass energy of 117.4 eV was used for the survey spectra. XPS depth profiling was achieved with an Ar ion sputtering source operated at an accelerating voltage of 2 kV. The contact angle was characterized using an OCA20 instrument (DataPhysics Instruments, Filderstadt, Germany).

4.5. Electrochemical Measurements. The electrochemical ORR activity was measured in a four-electrode cell using an Autolab bipotentiostat (PGSTAT204) and a Pine electrochemical system

(AFMSRCE rotator) on the RRDE. The RRDE electrode consisted of a glassy carbon disk (diameter: 5.61 mm; area: 0.2475 cm²) surrounded by a Pt ring (area: 0.1866 cm²) with a collection efficiency of 39.5%. A Pt wire was used as the counter electrode; Hg/HgO (RE-61AP, BAS) was used as the reference electrode in aqueous medium. All reported potentials refer to the reversible hydrogen electrode (RHE) potential. The potentials were converted to the RHE according to the equation

$$E_{(\text{RHE})} = E_{(\text{Hg}/\text{HgO})} + E_{(\text{Hg}/\text{HgO})}^{\circ} + 0.059 \text{ pH} \quad (5)$$

The electrochemical ORR performances of the catalysts were studied using CV and LSV. The electrochemical measurements were first implemented in N₂- and then O₂-saturated 0.1 M KOH. The electrolyte was deaerated by purging high-purity N₂ gas into the electrolyte for 60 min prior to each electrochemical measurement. For each catalyst tested, a cyclic voltammogram was first collected in N₂-saturated 0.1 M KOH from 0.10 to 1.10 V (vs RHE) at 100 mV s⁻¹ until a steady state cyclic voltammogram was obtained. For the ORR test, the electrolyte was purged with high-purity O₂ gas for at least 60 min to ensure O₂ saturation. LSV measurements during oxygen reduction were performed in O₂-saturated 0.1 M KOH by sweeping the potential cathodically from 0.99 to 0.18 V (vs RHE) at 10 mV s⁻¹ with the electrode rotated (0, 400, 900, 1200, and 1600 rpm) and O₂ gas purged into the solution at a flow rate of 25 standard cubic centimeters per minute (sccm). For all RRDE measurements, the ring potential was held at 1.40 V (vs RHE) to oxidize any HO₂⁻ produced in the alkaline solution.^{8,36} The percentage of HO₂⁻ produced and the transfer number (*n*) during the ORR were calculated using the equations^{8,14}

$$\% \text{HO}_2^- = 200X \frac{I_{\text{R}}/N}{I_{\text{D}} + I_{\text{R}}/N} \quad (6)$$

$$n = 4X \frac{I_{\text{D}}}{I_{\text{D}} + I_{\text{R}}/N} \quad (7)$$

where *I_R* is the ring current, *I_D* is the disk current, and *N* is the collection efficiency of the ring electrode (0.395). Stability tests were conducted using a chronoamperometric technique at a bias potential of 0.4 V (vs RHE) in O₂-saturated 0.1 M KOH at a rotation rate of 1600 rpm.

The electron transfer number for the ORR was derived from the Koutecky–Levich equation:^{50,52}

$$\frac{1}{j} = \frac{1}{j_{\text{k}}} + \frac{1}{j_{\text{d}}} = \frac{1}{j_{\text{k}}} + \frac{1}{B\omega^{1/2}} \quad (8)$$

where *j* is the measured disk current density; *j_k* and *j_d* are the kinetic and the diffusion limiting current densities, respectively; *B* is the so-called “B factor,” given by the equation⁵⁰

$$B = 0.62nFD_{\text{O}_2}^{2/3}\nu^{-1/6}C_{\text{O}_2} \quad (9)$$

where *n* is the apparent number of electrons transferred in the reaction, *F* is the Faraday constant (96 485 C mol⁻¹), *D_{O₂}* is the diffusion coefficient of O₂ (1.86 × 10⁻⁵ cm² s⁻¹), *ν* is the kinetic viscosity of the solution (0.01 cm² s⁻¹), *C_{O₂}* is the concentration of O₂ dissolved in the electrolyte (1.21 × 10⁻⁶ mol cm⁻³), and *ω* is the electrode rotation rate (rad s⁻¹)

■ ASSOCIATED CONTENT

Supporting Information

The Supporting Information is available free of charge at <https://pubs.acs.org/doi/10.1021/acsaem.9b02228>.

Monomer synthesis, electropolymerization current–time (*I*–*t*) curves, XRD patterns, FE-SEM images, XPS depth profiles, RRDE voltammograms, cyclic voltammograms, corresponding current–scan rate plots, and ORR performances (PDF)

■ AUTHOR INFORMATION

Corresponding Authors

Shyh-Chyang Luo – National Taiwan University, Taipei, Taiwan, and Advanced Research Center of Green Materials Science & Technology, Taipei, Taiwan;

ORCID: orcid.org/0000-0003-3972-1086;

Email: shyhchyang@ntu.edu.tw

Yuan-Chung Cheng – Academia Sinica and National Taiwan University, Taipei, Taiwan, and National Taiwan University, Taipei, Taiwan; ORCID: orcid.org/0000-0003-0125-4267;

Email: yuanchung@ntu.edu.tw

Hsiao-hua Yu – Academia Sinica, Nankang, Taipei, Taiwan, Academia Sinica and National Taiwan University, Taipei, Taiwan, Academia Sinica, Taipei, Taiwan, and National Chiao Tung University, Hsinchu, Taiwan; ORCID: orcid.org/0000-0002-3603-6932;

Email: bruceyu@gate.sinica.edu.tw

Other Authors

Tharwat Hassan Mansoure – Academia Sinica, Nankang, Taipei, Taiwan, Academia Sinica and National Taiwan University, Taipei, Taiwan, National Taiwan University, Taipei, Taiwan, and Assiut University, Assiut, Egypt; ORCID: orcid.org/0000-0002-5848-0196

Hailemichael Ayalew – Academia Sinica, Nankang, Taipei, Taiwan, and National Chiao Tung University, Hsinchu, Taiwan

Wei-Lun Kao – Academia Sinica, Taipei, Taiwan

Jing-Jong Shyue – Academia Sinica, Taipei, Taiwan;

ORCID: orcid.org/0000-0002-8508-659X

Complete contact information is available at:

<https://pubs.acs.org/doi/10.1021/acsaem.9b02228>

Notes

The authors declare no competing financial interest.

■ ACKNOWLEDGMENTS

We thank the SPROUT Project, including the Center for Emergent Functional Matter Science of National Chiao Tung University and Advanced Research Center for Green Materials Science and Technology, funded by the Ministry of Education (108L9006) and the Ministry of Science and Technology of Taiwan (Grants MOST 107-3017-F009-003 and 108-3017-F-002-002) for financial support.

■ REFERENCES

- (1) Steeneveldt, R.; Berger, B.; Torp, T. A. CO₂ Capture and Storage Closing the Knowing–Doing Gap. *Chem. Eng. Res. Des.* **2006**, *84*, 739–763.
- (2) Metz, B.; Davidson, O.; Coninck, H.; Loss, M.; Meyer, L. *IPCC Special Report on Carbon Dioxide Capture and Storage*; Cambridge University Press: Cambridge, U.K., 2005.
- (3) Debe, M. K. Electrocatalyst Approaches and Challenges for Automotive Fuel Cells. *Nature* **2012**, *486*, 43–51.
- (4) Elezovic, N. R.; Radmilovic, V. R.; Krstajic, N. V. Platinum Nanocatalysts on Metal Oxide Based Supports for Low Temperature Fuel Cell Applications. *RSC Adv.* **2016**, *6*, 6788–6801.
- (5) Li, M.; Zhao, Z.; Cheng, T.; Fortunelli, A.; Chen, C.-Y.; Yu, R.; Zhang, Q.; Gu, L.; Merinov, B. V.; Lin, Z.; Zhu, E.; Yu, T.; Jia, Q.; Guo, J.; Zhang, L.; Goddard, W. A., III; Huang, Y.; Duan, X. Ultrafine

Jagged Platinum Nanowires Enable Ultrahigh Mass Activity for the Oxygen Reduction Reaction. *Science* **2016**, *354*, 1414–1419.

(6) Gasteiger, H. A.; Kocha, S. S.; Sompalli, B.; Wagner, F. T. Activity Benchmarks and Requirements for Pt, Pt-Alloy, and Non-Pt Oxygen Reduction Catalysts for PEMFCs. *Appl. Catal., B* **2005**, *56*, 9–35.

(7) Li, G.; Wang, X.; Fu, J.; Li, J.; Park, M. G.; Zhang, Y.; Lui, G.; Chen, Z. Pomegranate-Inspired Design of Highly Active and Durable Bifunctional Electrocatalysts for Rechargeable Metal–Air Batteries. *Angew. Chem., Int. Ed.* **2016**, *55*, 4977–4982.

(8) Qi, C.; Zhang, L.; Xu, G.; Sun, Z.; Zhao, A.; Jia, D. Co@Co₃O₄ Nanoparticle Embedded Nitrogen-Doped Carbon Architectures as Efficient Bicatals for Oxygen Reduction and Evolution Reactions. *Appl. Surf. Sci.* **2018**, *427*, 319–327.

(9) Ibrahim, K. B.; Tsai, M.-C.; Chala, S. A.; Berihun, M. K.; Kahsay, A. W.; Berhe, T. A.; Su, W.-N.; Hwang, B.-J. A Review of Transition Metal-Based Bifunctional Oxygen Electrocatalysts. *J. Chin. Chem. Soc.* **2019**, *66*, 829–865.

(10) Higgins, D. C.; Hoque, M. A.; Hassan, F.; Choi, J.-Y.; Kim, B.; Chen, Z. Oxygen Reduction on Graphene–Carbon Nanotube Composites Doped Sequentially with Nitrogen and Sulfur. *ACS Catal.* **2014**, *4*, 2734–2740.

(11) Zhao, D.; Liu, H.; Wu, X. Bi-interface Induced Multi-active MCo₂O₄@MCo₂S₄@PPy (M = Ni, Zn) Sandwich Structure for Energy Storage and Electrocatalysis. *Nano Energy* **2019**, *57*, 363–370.

(12) Morozan, A.; Jégou, P.; Campidelli, S.; Palacin, S.; Josselme, B. Relationship Between Polypyrrole Morphology and Electrochemical Activity Towards Oxygen Reduction Reaction. *Chem. Commun.* **2012**, *48*, 4627–4629.

(13) Silva, R.; Voiry, D.; Chhowalla, M.; Asefa, T. Efficient Metal-Free Electrocatalysts for Oxygen Reduction: Polyaniline Derived N- and O-Doped Mesoporous Carbons. *J. Am. Chem. Soc.* **2013**, *135*, 7823–7826.

(14) Wu, X.; Yao, S. Flexible Electrode Materials Based on WO₃ nanotube bundles for High Performance Energy Storage Devices. *Nano Energy* **2017**, *42*, 143–150.

(15) Kerr, R.; Pozo-Gonzalo, C.; Forsyth, M.; Winther-Jensen, B. Influence of the Polymerization Method on the Oxygen Reduction Reaction Pathway on PEDOT. *ECS Electrochem. Lett.* **2013**, *2*, F29–F31.

(16) Winther-Jensen, B.; Winther-Jensen, O.; Forsyth, M.; MacFarlane, D. High Rates of Oxygen Reduction over a Vapor Phase–Polymerized PEDOT Electrode. *Science* **2008**, *321*, 671–674.

(17) Arbizzani, C.; Mastragostino, M.; Rossi, M. Preparation and Electrochemical Characterization of a Polymer Li_{1.03}Mn_{1.97}O₄/PEDOT Composite Electrode. *Electrochem. Commun.* **2002**, *4*, 545–549.

(18) Vigil, J. A.; Lambert, T. N.; Eldred, K. Electrodeposited MnO_x/PEDOT Composite Thin Films for the Oxygen Reduction Reaction. *ACS Appl. Mater. Interfaces* **2015**, *7*, 22745–22750.

(19) Vigil, J. A.; Brumbach, M. T.; Duay, J.; Lambert, T. N. Insights into the Spontaneous Formation of Hybrid PdO_x/PEDOT Films: Electroless Deposition and Oxygen Reduction Activity. *RSC Adv.* **2018**, *8*, 24428–24433.

(20) Vigil, J. A.; Lambert, T. N.; Kelly, M.; Aidun, R. Hybrid PEDOT/MnO_x Nanostructured Electrocatalysts for Oxygen Reduction. *Mater. Chem. Front.* **2017**, *1*, 1668–1675.

(21) Drillet, J.-F.; Dittmeyer, R.; Jüttner, K.; Li, L.; Mangold, K.-M. New Composite DMFC Anode with PEDOT as a Mixed Conductor and Catalyst Support. *Fuel Cells* **2006**, *6*, 432–438.

(22) Li, Y.; Liu, Y.; Fan, L.; Yuan, G.; Han, J.; Guo, R. Doped Nanocarbons Derived from Conducting Polymers toward ORR Electrocatalysts. *Adv. Sustainable Syst.* **2018**, *2*, 1800033–1800047.

(23) Abdelhamid, M. E.; Snook, G. A.; O'Mullane, A. P. Electropolymerisation of Catalytically Active PEDOT from an Ionic Liquid on a Flexible Carbon Cloth using a Sandwich Cell Configuration. *ChemPlusChem* **2015**, *80*, 74–82.

(24) Muhamad, N. B.; Khairul, W. M.; Yusoff, F. Synthesis and Characterization of Poly(3,4-ethylenedioxythiophene) Functionalized

Graphene with Gold Nanoparticles as a Potential Oxygen Reduction Electrocatalysts. *J. Solid State Chem.* **2019**, *275*, 30–37.

(25) Tintula, K. K.; Sahu, A. K.; Shahid, A.; Pitchumani, S.; Sridhar, P.; Shukla, A. K. Mesoporous Carbon and Poly(3,4-ethylenedioxythiophene) Composite as Catalysts Support for Polymer Electrolyte Fuel Cells. *J. Electrochem. Soc.* **2010**, *157*, B1679–B1685.

(26) Su, C.-H.; Sun, C.-L.; Liao, Y.-C. Printed Combinatorial Sensors for Simultaneous Detection of Ascorbic Acid, Uric Acid, Dopamine, and Nitrite. *ACS Omega* **2017**, *2*, 4245–4252.

(27) Liu, D.; Wang, Q.; Elinski, M.; Chen, P.; Traverse, C. J.; Yang, C. Ultrathin Hole Extraction Layer for Efficient Inverted Perovskite Solar Cells. *ACS Omega* **2018**, *3*, 6339–6345.

(28) Li, Y.; Wu, Y.; Zeng, W.; Li, Y.; Xu, L.; Qiu, X.; Chen, R.; Huang, W. Improving Efficiency of Blue Organic Light-Emitting Diode with Sulfoethylated Lignin Doped PEDOT as Anode Buffer Layer. *ACS Sustainable Chem. Eng.* **2016**, *4*, 2004–2011.

(29) Österholm, A. M.; Ponder, J. F.; Kerszulis, J. A.; Reynolds, J. R. Solution Processed PEDOT Analogues in Electrochemical Supercapacitors. *ACS Appl. Mater. Interfaces* **2016**, *8*, 13492–13498.

(30) Amanchukwu, C. V.; Gauthier, M.; Batcho, T. P.; Symister, C.; Shao-Horn, Y.; D'Arcy, J. M.; Hammond, P. T. Evaluation and Stability of PEDOT Polymer Electrodes for Li–O₂ Batteries. *J. Phys. Chem. Lett.* **2016**, *7*, 3770–3775.

(31) Yoon, S. H.; Park, Y. J. Air Electrode Based on Poly(3,4-ethylenedioxythiophene) Microflower/Graphene Composite for Superior Li–O₂ Batteries with Excellent Cycle Performance. *RSC Adv.* **2017**, *7*, 56752–56759.

(32) Jia, X.; Ge, Y.; Shao, L.; Wang, C.; Wallace, G. G. Tunable Conducting Polymers: Toward Sustainable and Versatile Batteries. *ACS Sustainable Chem. Eng.* **2019**, *7*, 14321–14340.

(33) Lind, J. U.; Hansen, T. S.; Daugaard, A. E.; Hvilsted, S.; Andresen, T. L.; Larsen, N. B. Solvent Composition Directing Click-Functionalization at the Surface or in the Bulk of Azide-Modified PEDOT. *Macromolecules* **2011**, *44*, 495–501.

(34) Zhang, J.; Dai, L. Heteroatom-Doped Graphitic Carbon Catalysts for Efficient Electrocatalysis of Oxygen Reduction Reaction. *ACS Catal.* **2015**, *5*, 7244–7253.

(35) Guo, Z.; Qiao, Y.; Liu, H.; Ding, C.; Zhu, Y.; Wan, M.; Jiang, L. Self-Assembled Hierarchical Micro/Nanostructured PEDOT as an Efficient Oxygen Reduction Catalyst over a Wide pH Range. *J. Mater. Chem.* **2012**, *22*, 17153–17158.

(36) Zhang, M.; Yuan, W.; Yao, B.; Li, C.; Shi, G. Solution-Processed PEDOT:PSS/Graphene Composites as the Electrocatalyst for Oxygen Reduction Reaction. *ACS Appl. Mater. Interfaces* **2014**, *6*, 3587–3593.

(37) Li, J.; Li, Z.; Ning, F.; Zhou, L.; Zhang, R.; Shao, M.; Wei, M. Ultrathin Mesoporous Co₃O₄ Nanosheet Arrays for High-Performance Lithium-Ion Batteries. *ACS Omega* **2018**, *3*, 1675–1683.

(38) Zhao, D.; Dai, M.; Liu, H.; Xiao, L.; Wu, X.; Xia, H. Constructing High Performance Hybrid Battery and Electrocatalyst by Heterostructured NiCo₂O₄@NiWS Nanosheets. *Cryst. Growth Des.* **2019**, *19*, 1921–1929.

(39) Wang, Y.; Zhou, T.; Jiang, K.; Da, P.; Peng, Z.; Tang, J.; Kong, B.; Cai, W.-B.; Yang, Z.; Zheng, G. Reduced Mesoporous Co₃O₄ Nanowires as Efficient Water Oxidation Electrocatalysts and Supercapacitor Electrodes. *Adv. Energy Mater.* **2014**, *4*, 1400696–1400702.

(40) Xia, X. H.; Tu, J. P.; Zhang, J.; Xiang, J. Y.; Wang, X. L.; Zhao, X. B. Fast Electrochromic Properties of Self-Supported Co₃O₄ Nanowire Array Film. *Sol. Energy Mater. Sol. Cells* **2010**, *94*, 386–389.

(41) Makimura, Y.; Rougier, A.; Tarascon, J.-M. Cobalt and Tantalum Additions for Enhanced Electrochromic Performances of Nickel-Based Oxide Thin Films Grown by Pulsed Laser Deposition. *Appl. Surf. Sci.* **2006**, *252*, 4593–4598.

(42) Xia, X.; Chao, D.; Qi, X.; Xiong, Q.; Zhang, Y.; Tu, J.; Zhang, H.; Fan, H. J. Controllable Growth of Conducting Polymers Shell for Constructing High-Quality Organic/Inorganic Core/Shell Nanostructures and their Optical–Electrochemical Properties. *Nano Lett.* **2013**, *13*, 4562–4568.

- (43) Mandal, S.; Rakibuddin, M.; Ananthkrishnan, R. Strategic Synthesis of SiO₂-Modified Porous Co₃O₄ Nano-Octahedra Through the Nanocoordination Polymer Route for Enhanced and Selective Sensing of H₂ Gas over NO_x. *ACS Omega* **2018**, *3*, 648–661.
- (44) Zhao, D.; Dai, M.; Tong, Y.; Song, X.; Wu, X. Mixed Transition Metal Oxide Nanowire Arrays Enabling Hybrid Capacitor Performance Enhancement. *CrystEngComm* **2019**, *21*, 5789–5796.
- (45) Ortiz-Quinonez, J.-L.; Pal, U. Borohydride-Assisted Surface Activation of Co₃O₄/CoFe₂O₄ Composite and Its Catalytic Activity for 4-Nitrophenol Reduction. *ACS Omega* **2019**, *4*, 10129–10139.
- (46) Zhang, M.; Li, R.; Chang, X.; Xue, C.; Gou, X. Hybrid of Porous Cobalt Oxide Nanospheres and Nitrogen-Doped Graphene for Applications in Lithium-Ion Batteries and Oxygen Reduction Reaction. *J. Power Sources* **2015**, *290*, 25–34.
- (47) Miao, Y.-E.; Li, F.; Lu, H.; Yan, J.; Huang, Y.; Liu, T. Nanocubic-Co₃O₄ Coupled with Nitrogen-Doped Carbon Nanofiber Network: A Synergistic Binder-Free Catalyst Toward Oxygen Reduction Reactions. *Compos. Commun.* **2016**, *1*, 15–19.
- (48) Xiao, X.; Liu, X.; Zhao, H.; Chen, D.; Liu, F.; Xiang, J.; Hu, Z.; Li, Y. Facile Shape Control of Co₃O₄ and the Effect of the Crystal Plane on Electrochemical Performance. *Adv. Mater.* **2012**, *24*, 5762–5766.
- (49) Liu, H.; Long, W.; Song, W.; Liu, J.; Wang, F. Tuning Electronic Band Gap: An Efficient Way to Improve Electrocatalytic Activity of Carbon-Supported Co₃O₄ Nanocrystals for Oxygen Reduction Reaction. *Chem. - Eur. J.* **2017**, *23*, 2599–2609.
- (50) Huang, Y.; Miao, Y. E.; Lu, H.; Liu, T. Hierarchical ZnCo₂O₄@NiCo₂O₄ Core–Sheath Nanowires: Bifunctionality Towards High-Performance Supercapacitors and the Oxygen-Reduction Reaction. *Chem. - Eur. J.* **2015**, *21*, 10100–10108.
- (51) Kumar, R.; Singh, L.; Zularisam, A. W.; Hai, F. I. Potential of Porous Co₃O₄ Nanorods as Cathode Catalyst for Oxygen Reduction Reaction in Microbial Fuel Cells. *Bioresour. Technol.* **2016**, *220*, 537–542.
- (52) Wang, M.; Huang, J.; Wang, M.; Zhang, D.; Zhang, W.; Li, W.; Chen, J. Co₃O₄ Nanorods Decorated Reduced Graphene Oxide Composite for Oxygen Reduction Reaction in Alkaline Electrolyte. *Electrochem. Commun.* **2013**, *34*, 299–303.
- (53) Odedairo, T.; Yan, X.; Ma, J.; Jiao, Y.; Yao, X.; Du, A.; Zhu, Z. Nanosheets Co₃O₄ Interleaved with Graphene for Highly Efficient Oxygen Reduction. *ACS Appl. Mater. Interfaces* **2015**, *7*, 21373–21380.
- (54) Chlistunoff, J.; Sansiñena, J.-M. On the Use of Nafion® in Electrochemical Studies of Carbon Supported Oxygen Reduction Catalysts in Aqueous Media. *J. Electroanal. Chem.* **2016**, *780*, 134–146.
- (55) Xiao, R.; Cho, S. I.; Liu, R.; Lee, S. B. Controlled Electrochemical Synthesis of Conductive Polymer Nanotube Structures. *J. Am. Chem. Soc.* **2007**, *129*, 4483–4489.
- (56) Chuang, T. J.; Brundle, C. R.; Rice, D. W. Interpretation of the X-ray Photoemission Spectra of Cobalt Oxides and Cobalt Oxide Surfaces. *Surf. Sci.* **1976**, *59*, 413–429.
- (57) Chuang, T. J.; Brundle, C. R.; Wandelt, K. An X-ray Photoelectron Spectroscopy Study of the Chemical Changes in Oxide and Hydroxide Surfaces Induced Ar⁺ Ion Bombardment. *Thin Solid Films* **1978**, *53*, 19–27.
- (58) Sun, X.; Zhang, Y.; Song, P.; Pan, J.; Zhuang, L.; Xu, W.; Xing, W. Fluorine-Doped Carbon Blacks: Highly Efficient Metal-Free Electrocatalysts for Oxygen Reduction Reaction. *ACS Catal.* **2013**, *3*, 1726–1729.
- (59) Shen, B.; Chen, J.; Yan, X.; Xue, Q. Synthesis of Fluorine-Doped Multi-Layered Graphene Sheets by Arc-Discharge. *RSC Adv.* **2012**, *2*, 6761–6764.
- (60) Zhao, D.; Dai, M.; Liu, H.; Chen, K.; Zhu, X.; Xue, D.; Wu, X.; Liu, J. *Adv. Mater. Interfaces* **2019**, *6* (21), 1901308–1901317.
- (61) Liu, H.; Zhao, D.; Liu, Y.; Hu, P.; Wu, X.; Xia, H. Boosting Energy Storage and Electrocatalytic Performances by Synergizing CoMoO₄@MoZn₂₂ Core-shell Structures. *Chem. Eng. J.* **2019**, *373*, 485–492.
- (62) Zhao, Y.; He, J.; Dai, M.; Zhao, D.; Wu, X.; Liu, B. Emerging CoMn-LDH@MnO₂ Electrode Materials Assembled Using Nanosheets for Flexible and Foldable Energy Storage Devices. *J. Energy Chem.* **2020**, *45*, 67–73.
- (63) Nansé, G.; Papirer, E.; Fioux, P.; Moguet, F. Fluorination of Carbon Blacks: An X-ray Photoelectron Spectroscopy Study: I. A Literature Review of XPS Studies of Fluorinated Carbons. XPS Investigation of Some References Compounds. *Carbon* **1997**, *35*, 175–194.
- (64) Lee, Y.-G.; Ahn, H.-J. Tri(Fe/N/F)-Doped Mesoporous Carbons as Efficient Electrocatalysts for the Oxygen Reduction Reaction. *Appl. Surf. Sci.* **2019**, *487*, 389–397.
- (65) Panomsuwan, G.; Saito, N.; Ishizaki, T. Simple One-Step Synthesis of Fluorine-Doped Carbon Nanoparticles as Potential Alternative Metal-Free Electrocatalysts for Oxygen Reduction Reaction. *J. Mater. Chem. A* **2015**, *3*, 9972–9981.
- (66) Wang, W.; Lv, F.; Lei, B.; Wan, S.; Luo, M.; Guo, S. Tuning Nanowires and Nanotubes for Efficient Fuel-Cell Electrocatalysis. *Adv. Mater.* **2016**, *28*, 10117–10141.
- (67) McCrory, C. C. L.; Jung, S.; Peters, J. C.; Jaramillo, T. F. Benchmarking Heterogeneous Electrocatalysts for the Oxygen Evolution Reaction. *J. Am. Chem. Soc.* **2013**, *135*, 16977–16987.
- (68) Makhlof, M. T.; Abu-Zied, B. M.; Mansoure, T. H. Direct Fabrication of Cobalt Oxide Nanoparticles Employing Glycine as a Combustion Fuel. *Phys. Chem.* **2012**, *2*, 86–93.
- (69) Wu, J. G.; Lee, C. Y.; Wu, S. S.; Luo, S. C. Ionic Liquid-Assisted Electropolymerization for Lithographical Perfluorocarbon Deposition and Hydrophobic Patterning. *ACS Appl. Mater. Interfaces* **2016**, *8*, 22688–22695.